A Salient Region Detection and Pattern Matching Based Algorithm for Center Detection of a Partially-Covered Tropical Cyclone in a SAR Image

Shaohui Jin[1], Shuang Wang[1], Xiaofeng Li[2], Licheng Jiao[1], Jun A. Zhang[3] and Dongliang Shen[4]

***Abstract*—Spaceborne microwave synthetic aperture radar (SAR), with its high spatial resolution, large area coverage, day/night imaging capability, and penetrating cloud capability, has been used as an important tool for tropical cyclone monitoring. The accuracy of locating tropical cyclone centers has a large impact on the accuracy of tropical cyclone track prediction. Usually the center of a tropical cyclone can be accurately located if the tropical cyclone eye is fully covered by a SAR image. In some cases, due to the limited coverage of the SAR, only a part of a tropical cyclone was imaged without the eye. From a SAR image processing point of view, these facts make the automatic center location of tropical cyclones a challenging work. This paper addresses the problem by proposing a semi-automatic center location method based on salient region detection and pattern matching. A salient region detection algorithm is proposed in which the salient region map contains mainly the rain bands of a tropical cyclone in a SAR image. The pattern matching problem is transformed into an optimization problem solved by using the particle swarm optimization algorithm (PSOA) to search the best estimated center of a tropical cyclone. To estimate the accuracy of the located center, we compare the results with the National Oceanic and Atmospheric Administration National Hurricane Center's Best Track Data. Experiments demonstrate that the proposed method achieves good accuracy for locating the centers of tropical cyclones from SAR images that do not contain a distinguishable eye signature.**

***Index Terms*—tropical cyclone, synthetic aperture radar, pattern matching, Particle Swarm Optimization algorithm (PSOA).**

Manuscript received XX; revised XX; accepted XX. The RADARSAT SAR images were provided by Canadian Space Agency. This work is supported in part by National Natural Science Foundation of China under Grants 41228007, 41201350, 61173092, and 61003198. It is also supported by the Program for New Century Excellent Talents in University under Grant NCET-11-0692, and the Fund for Foreign Scholars in University Research and Teaching Programs under Grant B07048. The views, opinions, and findings contained in this report are those of the authors and should not be construed as an official NOAA or U.S. Government position, policy, or decision.

S. H. Jin is with Key Laboratory of Intelligent Perception and Image Understanding of Ministry of Education, International Research Center for Intelligent Perception and Computation, Xidian University, Xi'an, Shaanxi Province 710071, China.

S. Wang is with Key Laboratory of Intelligent Perception and Image Understanding of Ministry of Education, International Research Center for Intelligent Perception and Computation, Xidian University, Xi'an, Shaanxi Province 710071, China(e-mail: shwang@mail.xidian.edu.cn).

X. F. Li is with the Global Science and Technology, National Oceanic and Atmospheric Administration (NOAA)/NOAA's Satellite and Information Service, College Park, MD 20740, USA.

L. C. Jiao is with Key Laboratory of Intelligent Perception and Image Understanding of Ministry of Education, International Research Center for Intelligent Perception and Computation, Xidian University, Xi'an, Shaanxi Province 710071, China.

J. A. Zhang is with Rosenstiel School of Marine and Atmospheric Science, University of Miami, and NOAA/AOML/Hurricane Research Division, Miami, Florida, USA.

D. L. Shen is with College of Marine Sciences, Shanghai Ocean University, Shanghai, China.

I. INTRODUCTION

TROPICAL cyclones may cause major disasters and have a strong destructive potential to bring significant personal and economic loss to coastal areas. The location of the center of a tropical cyclone is key information that is needed for timely and accurate tropical cyclone forecasting. It closely relates to the position and motion tendency of a tropical cyclone and is vital for prediction, to enable people to avoid or prevent disaster caused by strong winds and torrential rain.

Since the launch of the first polar-orbiting meteorological satellite in the early 1960s, remote sensing techniques have proved to be a useful method for tropical cyclone analyses and forecasting (e.g. [1]- [5]). Satellite cloud images, acquired by passive remote-sensing instruments operating in the visible and infrared (IR) bands, vividly describe cloud-level tropical cyclone horizontal structures with large area coverage and frequently repeated observations [6]. However, due to cloud cover and rain effects, the inner core structures and air-sea interaction near the ocean surface cannot be directly observed with visible or IR sensors. The microwave scatterometer is an active remote-sensing sensor. It works well at night and has a wide range of observation. In addition, it can simultaneously obtain wind speed and the wind direction of a wind field on the sea surface [7]. Weather radar is a kind of active microwave radar that emits radar pulses to the sky and then receives the radar backscatter. It can identify a tropical cyclone center based on echo signal intensity [8]. Data from the Tropical Rainfall Measuring Mission (TRMM)/Global Precipitation Measurement (GPM) can be used to research the precipitation

distribution or the intensity of a tropical cyclone (e.g. [9] and [10]).

Spaceborne synthetic aperture radar (SAR) has become another popular tool for tropical cyclone monitoring over recent years. This is a type of active microwave radar that emits radar pulses that can penetrate through clouds and then receive the radar backscatter from the Earth's surface. Therefore, SAR can take images of the Earth's surface and these images can reveal detailed structures of tropical cyclones on the ocean surface [1]. In addition, SAR has a high spatial resolution (10-100m) and can operate day and night under almost all weather conditions. Katsaros *et al.* (2002) discussed the usefulness of SAR in tropical cyclone monitoring [11]. Horstmann *et al.* (2005) studied sea surface tropical cyclone wind retrievals with RADARSAT-1 SAR with an existing geophysical model function, i.e., CMOD5 [12]. Yang *et al.* (2011) assessed the impact of radar calibration accuracy on the retrieval of wind speeds with a high degree of accuracy interpretation [13]. Recently, Li *et al.* (2013) systematically analyzed 83 typhoons and hurricanes observed in RADARSAT-1 and ENVISAT SAR images and manually extracted tropical cyclone morphology from these images [1]. These studies illustrate that extracting quantitative tropical cyclone information from SAR images has been a focus of research.

SAR images of tropical cyclones on the sea surface show the sea surface imprint of tropical cyclones and are related to the surface roughness affected by sea surface winds, rain roughening of the surface, waves and so on [14]. A complete tropical cyclone in a SAR image appears as bright-dark spiral patterns. There is almost no rain and wind within a tropical cyclone eye area, so the radar backscattering from this part of the sea surface is relatively weak compared to signal returns from other areas in a tropical cyclone. High winds and rain result in a brighter area around the eye wall. Therefore, for the tropical cyclone center eye detection, Du *et al.* (2003) proposed a wavelet analysis method to extract tropical cyclone eye shape and size [6], Jin *et al.* (2014) proposed a labeled watershed segmentation method to extract the hurricane eye and compared automatic extraction results with manual extraction results [15]. Recently, Zheng *et al.* (2016) extracted typhoon eyes in SAR images using two newly developed algorithms and showed good results when validated against the tropical cyclone best track data sets [16].

However, not every tropical cyclone has an obvious eye feature in a SAR image. There may even be no eye where a tropical cyclone is in the developing period or the declining period. Sometimes limited by the capture range of radar, a SAR image may contain parts of a tropical cyclone without an eye. Generally speaking, methods to estimate the center of a tropical cyclone automatically or semi-automatically fall into two categories: wind field analysis and pattern matching. Wind vector fields need a sequence of images. However, SAR provides only a single snap view at a time and therefore it is difficult to determine the wind direction from a single image. Pattern matching methods can be performed using only a single image. So we considered estimating the center position with a pattern matching method. Researchers have previously tried to locate the center of tropical cyclones using pattern matching methods in satellite cloud images that do not contain eye information. Wang *et al.* (2006) developed an auto-center-locating algorithm based on Hough transform [17]. They first locate the rain bands using image segmentation and mathematic morphology, and then match the skeleton lines of rain bands with a logarithm spiral using Hough transform. Segmentation methods such as threshold segmentation are used here to obtain the rain bands of a tropical cyclone from a SAR image. This is a straightforward but not very effective approach as rain bands cannot be distinguished from clouds with a similar reflectivity. Besides, the Hough transform has its limitations such as large calculations and poor detection performance when there is noise in an image. Xu *et al.* (2009) proposed a spiral rain band segmentation method by transforming it to the problem of classification with a support vector machine [18]. However, samples are chosen manually in this method. Wong *et al.* (2005) proposed a tropical cyclone eye fixing method using a genetic algorithm with temporal information [19]. Later in 2008, they developed a more automatic framework for tropical cyclone eye fixing with a method using a genetic algorithm [20]. Good results indicate that this genetic algorithm is robust and can be widely used. However, the extraction of regions of interest (the positions where the centers of the tropical cyclones may lie) needs the assistance of the previous image or forecaster. Moreover, the matching model used in the above work is a logarithm spiral, which looks similar to the geometrical structure of tropical cyclones but is not suitable for the accurate matching of diverse tropical cyclones. Besides, the matching of a logarithm spiral needs precise extraction of skeleton lines.

Taking advantage of the characteristics of tropical cyclones in SAR images, we developed a semi-automatic tropical cyclone center location method by combining our proposed salient region detection method with a particle swarm optimization algorithm (PSOA). The algorithm flowchart is shown in Fig. 1, and it mainly contains three steps. Step 1), rain bands are extracted using a salient region detection algorithm. Firstly, we calculate the standard deviation of gray values of image patches and get a gray value contrast feature map. Secondly, we calculate the Gabor features of a denoised tropical cyclone image and combine different orientation maps into a Gabor feature map. Thirdly, we combine the gray value contrast feature map and the Gabor feature map by weights to get the salient region map. Rain bands are mainly contained in the salient region map Step 2), the salient region map is segmented into a binary image and rain bands are selected by two filter criteria. Then we extract the skeleton lines. To get smooth lines for better matching, we apply expansion operators and pruning before and after the extraction. Step 3), we transform the matching problem into an optimization problem, and then apply the PSOA to estimate the optimum solution, which corresponds to the center of the tropical cyclone. To estimate the correctness of the located center, we compare the results with the National Oceanic and Atmospheric Administration National Hurricane Center's Best Track Data

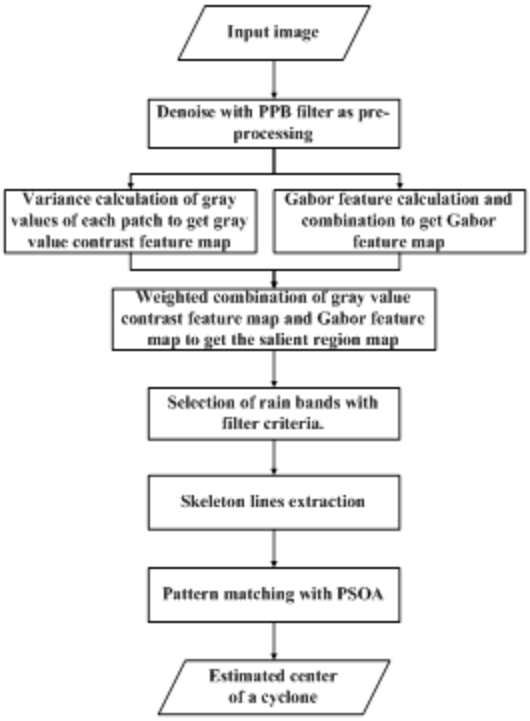

Fig. 1. A flowchart of our method.

sets. Experiments demonstrate that the proposed image processing method can correctly locate a tropical cyclone center in a SAR image with good accuracy. There are several parameters that need to be tuned. This semi-automatic method makes use of the gray level information and orientation information of a SAR image while does not require other observational data. At this point, although it is impossible to propose a fully-automatic image processing method to complete the same task, we will consider solving the challenging problem by combining data from other instruments.

The rest of the paper is organized as follows. Section 2 details our method. Experiment results using a set of RADARSAT-1 SAR images and comparison of the PSOA results and GA results are presented to verify the efficiency of our method in section 3. The conclusion is given in section 4.

II. Salient Region Detection And Pattern Matching Based SAR Image Processing Algorithm

In this section we introduce our three-step method to locate the center of a partially-covered tropical cyclone in a SAR image. Before the three-step procedure is applied, the tropical cyclone SAR image is denoised with a Probabilistic Patch-Based filter (PPB filter) [21]. Speckle noise in SAR is a type of multiplicative noise that reduces the actual resolution of the SAR image, and may affect target identification and sometimes cause features to disappear in the image. The existence of speckle noise makes extracting useful information directly from the SAR image difficult. So de-noising of the tropical cyclones SAR images is necessary. The PPB filter, which is considered as one of the best SAR image denoising method in recent years, can effectively remove the speckle noise in the homogeneous regions while preserving edges and shapes at the same time.

A. Salient Region Detection Algorithm to Produce a Rain-Band Map

The automatic center location of tropical cyclones without eyes using pattern matching methods usually needs the help of rain band information. Therefore we need to obtain the spiral information of rain bands before matching. Researchers often segment satellite cloud images using a threshold segmentation method [17] [19] [20]. These algorithms usually work well when the gray levels of the rain bands are obviously different from the gray levels of other regions. This is easy but not very effective when the gray levels of rain bands are more or less the same as those of other cloud clusters, which makes it hard to distinguish rain bands from other cloud clusters. Besides, influencing factors such as speckle noise, various configurations of tropical cyclone images acquired by different SAR instruments with different polarization, azimuth and spatial resolution, etc will make automatic segmentation of large numbers of rain bands more difficult. In addition, a tropical cyclone SAR image shows the sea surface imprint of a tropical cyclone with little texture information. Therefore we consider obtaining rain bands by salient region detection.

In computer vision, salient regions are defined as regions that attract human visual attention at the earliest visual processing when looking at an image. Salience is based on a variety of visual stimulation, such as color, brightness, texture, shape, edge, etc. High contrast between stimuli creates space reorganization of the receptive field cells, attracting the attention of the observer. That is the occurrence of the salience (e. g. [22]-[24]). People tend to rapidly search for the most important parts and ignore the less important parts when they watch an image based on vision task and their prior knowledge. This selective attention mechanism enables people to efficiently capture the areas that they are interested in. These captured areas can be called the focus of attention areas [25] or salient regions [26].

Since Itti and Koch proposed a model of saliency-based visual attention based on the human visual attention selective mechanism [27], visual salient region detection has become a popular research topic and many methods have been proposed (e. g. [27]-[37]). Although different saliency detection methods are based on different hypotheses different theories, they all have one common characteristic: they focus on the "center-surround" difference. For a tropical cyclone SAR image, the major characteristic that makes a tropical cyclone different from its surroundings is the gray values contrast and its special spiral structure associated with rain bands, so the gray values contrast and orientation information can be used for salient region detection. Besides, little texture information in a tropical cyclone SAR image is propitious to salient region detection based contrast. Based on these advantages we propose a salient region detection method based on gray value contrast and orientation information.

Standard deviation, the average value of the distances from each data set to the mean value in a data set, reflects the degree of the discrete degree of the data set. Given an image patch, if the standard deviation of the gray values of the pixels is large, the contrast of the adjacent pixels is also large. This means the gray values change greatly and there may be context change in the image patch. As mentioned above, the gray values of clouds of a tropical cyclone are different from those of its surrounding background in a tropical cyclone SAR image. So we can consider that the salient spiral structure is next to, or contained in, the regions with a large standard deviation. We can divide an image into patches with a sliding window, whose step is half of its side length. We can then calculate the standard deviation of each patch. Generally, the standard deviation of a patch containing two or more kinds of homogenous regions is larger than that of a patch containing only one kind of homogenous region. So a patch with a larger standard deviation can be considered more salient. Fig. 2 shows patches with different standard deviations. As shown, patch P1 is a homogenous region where the values of the pixels are more or less the same, so its standard deviation is small. But there is a context change in patch P2 and the values of the pixels in it are different, so its standard deviation is large. The larger the standard deviation, the more salient the corresponding patch. We get a gray value contrast feature map after normalization of all the standard deviations.

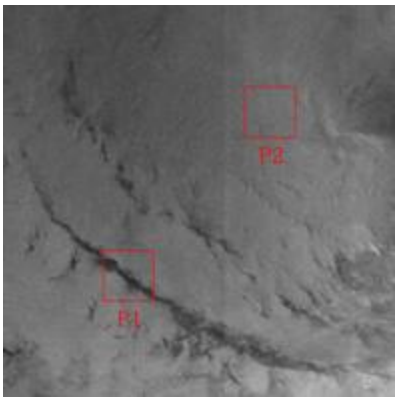

Fig. 2. Different patches with different standard deviation. Patch P1 passes through an edge of a rain band and contains a part of the rain band and a part of the background. Gray values of the two parts are different. Patch P2 only contains a part of the background, whose gray values are more or less the same. So Patch P1 has a bigger standard deviation than patch P2.

Since there are some irrelevant patterns whose gray values are similar to these of the rain bands, we may not extract the exact salient region only with gray value information. We further look at the spiral structure of rain bands that contain obvious orientation information. So we also make use of orientation information with Gabor features to improve the degree of saliency.

A 2D Gabor filter was first applied by Daugman [38] in the field of computer vision. The 2D Gabor filter has a visual characteristic and biology background. It can be seen as a good approximation to the sensitivity profiles of neurons found in the visual cortex of higher vertebrates [39]. The Gabor features have good directional characteristics that are sensitive to edge information. The Gabor filter will respond strongest if the filter's orientation is consistent with the orientation of specific features in an image. In addition, it is good at multi-frequencies and in multi-orientations, and is non-sensitive to light change. These advantages make the Gabor filter widely used in visual information extraction, pattern recognition and image processing. The 2D Gabor filter can be written as:

$$h(x,y) = \frac{1}{2\pi\sigma^2}\exp\left(-\frac{x'^2+y'^2}{2\sigma^2}\right)\exp\left[2\pi j(Ux'+Vy')\right] \quad (1)$$

Where $x' = x\cos\theta + y\sin\theta$ and $y' = y\cos\theta - x\sin\theta$, θ is the orientation, σ is the scaling parameters of the filter and (U,V) is the center frequency. The Gabor filter has good direction selectivity in the spatial domain and frequency selectivity in the frequency domain by choosing different directions and adjusting the frequency. The Gabor feature of an image $I(x,y)$ is the convolution of the image and the Gabor filter $h(x,y)$.

We calculate the Gabor features of a tropical cyclone SAR image in four orientations $(0^\circ, 45^\circ, 90^\circ, 135^\circ)$. Then the Gabor feature map is obtained by combining the four orientation maps with weights. Regions with high gray values in the Gabor feature map have more directional information. Then we combine the Gabor feature map and the gray value contrast feature map with different weighting to construct the final salient region map.

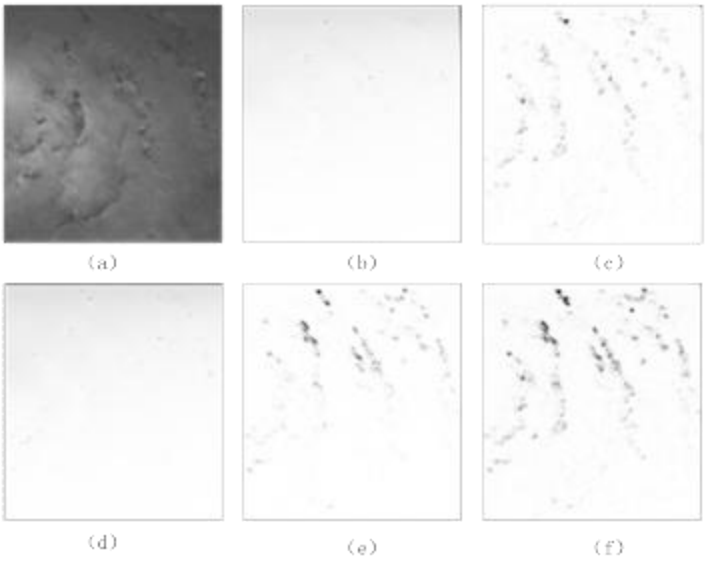

Fig. 3. Gabor feature maps of different orientations for a Cyclone SAR image. (a) A cyclone SAR image. (b), (c), (d), (e): Gabor feature maps when the orientation are 0°, 45°, 90° and 135°. When the orientation are 0° and 90°, the rain bands are disappeared or fuzzy. While when the orientations are 45° and 135°, the rain bands are obvious. (f): The combined Gabor feature map.

B. *Rain Bands Selection with Two Filter Criteria*

After the salient region detection, outlined in the previous section, the salient region map of a SAR tropical cyclone image is obtained. Regions with high gray values in the salient map are mainly rain bands. The skeleton lines of rain bands make their spiral shape and rolling tendency intuitive and visual. It is easy to understand and convenient to process spiral information by computer. So in this section we consider how to extract the correct skeleton lines of rain bands for pattern matching.

First of all, we need to get rain bands which have an obvious shape characteristic. Salient region detection has eliminated most of the irrelevant parts of the image. Regions with high gray values in the salient map are mainly rain bands. However, there are other irrelevant minor features, too. The combination of several minor features may also reflect a spiral tendency, but their skeleton lines are not continuous. Therefore, they cannot be used for pattern matching. To avoid the interference of minor regions, we segment the salient region map of a SAR tropical cyclone image into a binary image by a threshold, and then remove regions with small areas in the binary image with two filter criteria. So the first filter criterion is by area of region. We calculate the area of each region in the binary image, arrange them in order of area and only keep the several largest regions. Small regions are deleted with the first filter criterion. The second filter criterion evaluates the distance of the left-top point and the right-bottom point of a remained region. Several regions with the longest distances can be remained. We remain the one region with the longest distance for automatic computation. As shown in Fig. 6(g) - Fig. 11(g), regions with long and thin strips are kept when the second filter criterion was applied.

C. Skeleton Lines Extraction with Morphology and Pruning

The edges of the rain bands in a SAR image are irregular with protrusions and hollows. If we extract skeleton lines directly, it will contain branches. If there are holes in the rain band regions, the skeleton line will contain circular rings. All these conditions will affect the continued pattern matching. Here we take two measures to obtain smooth skeleton lines. Firstly, the rain bands are expanded using morphologic operators before extraction of the skeleton lines [40]. The hollows are filled and the edges of the connecting domains are smoothed, reducing the possibility of the skeleton lines forking. Secondly, the little branches and protrusions of the skeleton lines are pruned [41]. The two steps can be iterated if necessary. As shown in Fig. 6(i) - Fig. 11(i), the skeleton lines are smooth without additional branches, while the spiral shape of the original connected domains is preserved.

D. Particle Swarm Optimization Algorithm to Estimate Tropical Cyclone Centers Based on Pattern Matching

We focus on pattern matching to estimate tropical cyclone centers in this section. Here we choose an analytical model of two-dimensional surface storm-relative inflow angle in a tropical cyclone to estimate tropical cyclone centers. Zhang *et al.* (2012) presented an analysis of near-surface inflow angles using wind observation data from over 1600 quality-controlled global positioning system dropwindsondes deployed by aircraft on 187 flights into 18 hurricanes and proposed a parametric model of inflow angle based on these observations and analysis [42]. Here the inflow angle α_{SR} can be defined as the arctangent of the ratio of radial wind component v_r to tangential wind component v_t. Analysis results in the reference indicate a statistically significant dependence of inflow angle on the radial distance from the tropical cyclone center.

The model is defined as follows:

$$\alpha_{SR}(r^*, \theta, V_{max}, V_s) = A_{\alpha 0}(r^*, V_{max}) + A_{\alpha 1}(r^*, V_s, V_{max}) \cdot \cos[\theta - P_{\alpha 1}(r^*, V_s)] + \varepsilon \quad (2)$$

where θ is the azimuth angle measured clockwise from tropical cyclone motion direction, V_{max} is the maximum wind speed, V_s is the tropical cyclone motion speed and ε is the model error. $r^* = \frac{r}{R_{max}}$, where r is the radial distance measured in a polar coordinate system and R_{max} is the radial distance of maximum wind speed. $A_{\alpha 0}$, $A_{\alpha 1}$ and $P_{\alpha 1}$ are defined as:

$$A_{\alpha 0} = a_{A0} r^* + b_{A0} V_{max} + c_{A0} \quad (3)$$

$$A_{\alpha 1} = -A_{\alpha 0}(a_{A1} r^* + b_{A1} V_s + c_{A1}) \quad (4)$$

$$P_{\alpha 1} = a_{P1} r^* + b_{P1} V_s + c_{P1} \quad (5)$$

The coefficients (a, b, c) are shown in Table 1. The above inflow angle model is developed based on a subset of the full observation sample and he coefficients of $A_{\alpha 0}$ is the most accurately estimated quantity while the coefficients of $A_{\alpha 1}$ is the least.

TABLE I
PROPERTIES COEFFICIENTS FOR THE INFLOW ANGLE MODEL IN EQUATION (3) (4) (5).

Equation	Variables	a	b	c
(3)	A_{α_0}	-0.90	-0.90	-14.33
(4)	A_{α_1}	0.04	0.05	0.14
(5)	P_{α_1}	6.88	-9.60	85.31

Given the skeleton line l_{ske} of a rain band, we can obtain all the pixels $\{(x_i, y_i) | (x_i, y_i) \in l_{ske}\}$ on it. r_i is the Euclidean distance from one point (x_i, y_i) on the skeleton line to the center of the tropical cyclone (x_c, y_c) which we want to get. We can define the normalized distance r_i^* as:

$$r_i^* = \frac{\sqrt{(x_i - x_c)^2 + (y_i - y_c)^2}}{\sqrt{(x_{max} - x_c)^2 + (y_{max} - y_c)^2}} \quad (6)$$

where (x_{max}, y_{max}) is the position of the maximal wind speed. The corresponding azimuth can be defined as:

$$\theta_i = \arctan\left(\frac{y_i - y_c}{x_i - x_c}\right) \quad (7)$$

Given a tropical cyclone wind speed data, we can get the information about the maximal wind speed V_{max} and its position (x_{max}, y_{max}) and the tropical cyclone motion speed V_s. If we also know the center (x_c, y_c) of a tropical cyclone, we can get r^* and θ. Then the inflow angles can be determined with parameters $(r^*, \theta, V_{max}, V_s)$.

If the inflow angle values along a skeleton line are known, the key to solve the matching problem is to find the best combination of parameters (x_c, y_c) which makes the calculated inflow angles using formula (2) best match the given inflow angles. We can then treat the matching problem as an optimization problem. A candidate combination of parameters (x_{c_i}, y_{c_i}) corresponds to an estimated inflow angle set. When we find the optimal combination of parameters $(x_{c_{best}}, y_{c_{best}})$, the estimated inflow angles are closest to the given inflow angles. It means the optimal $(x_{c_{best}}, y_{c_{best}})$ is closest to the real tropical cyclone center. So the optimization problem here is to

find the optimal $(x_{c_{best}}, y_{c_{best}})$ on a skeleton-line image.

As mentioned in Section 1, the simple and easy Hough transform was often used as the matching method in previous work [17]. However, it only performs well on part of the matching pixels, and it is difficult to reach a good matching result. Wong *et al*. used a genetic algorithm to match skeleton lines with a logarithm spiral [19]. The genetic algorithm is robust and has global search ability. However, the crossover operator and mutation operator of the genetic algorithm guide the search iterative process randomly. So they provide the opportunity to evolve but inevitably produce the possibility of degradation at the same time. There will be a lot of redundant iteration when the solution reaches a certain range, resulting in a low efficiency of exact solutions.

Different from the genetic algorithm, the Particle Swarm Optimization algorithm (PSOA) proposed by Eberhart and Kennedy [43] is simpler and more effective with fewer input parameters required. The calculation converges to the optimal solution quicker. These advantages make the PSOA widely used in optimization problems (e. g. [44]-[47]). We chose the PSOA to search the optimum solution to solve the matching problem.

The PSOA is based on research of birds' predation. We suppose that a flock of birds is searching for food randomly. If there is only one piece of food, the easiest but most effective

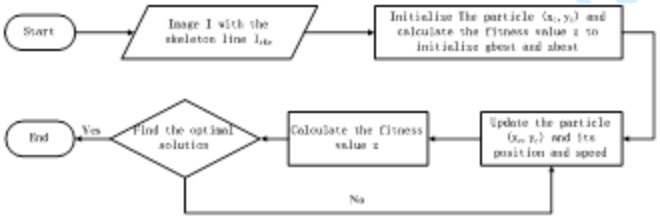

Fig. 4. Scheme of the PSOA.

strategy to find the food is to search the surrounding area of the bird which is nearest to the food. This idea is used in the PSOA. Here we can consider the best center (x_c, y_c) as the food. A solution (an estimated center) for the optimization problem is considered to be the position of a bird, which is also called a particle. The method involves in inputting a binary image of skeleton lines, counting the number of lines and getting all the pixel positions of each skeleton line. Then it is necessary to initialize the position and speed of the original searching particle (parameters (x_c, y_c)). Every particle has its own position and speed, which determines its direction and distance of flight. The current position of each particle is initialized as its original best position (it can be called pbest). There is a fitness value determined by a fitness function. The corresponding fitness value z of each particle is calculated using the fitness function. The best fitness value is considered to be the global fitness value. The global best position is initialized (it can be called gbest) with the position of the particle having the best fitness value. Then each particle adjusts its speed and position according to gbest and its own speed and position. The fitness value z of each particle is calculated. If the fitness value of one particle is better than its current pbest, the current pbest moves into its position. If the best pbest of all particles is better than the current gbest, move the current gbest into the position of the particle having the best pbest. The process reiterates until the optimum solution is found or the iterative time has been reached.

A matching result can be evaluated by the degree of error between a given inflow angle α_{SR} and the estimated inflow angle α. The smaller the error is, the better the matching result

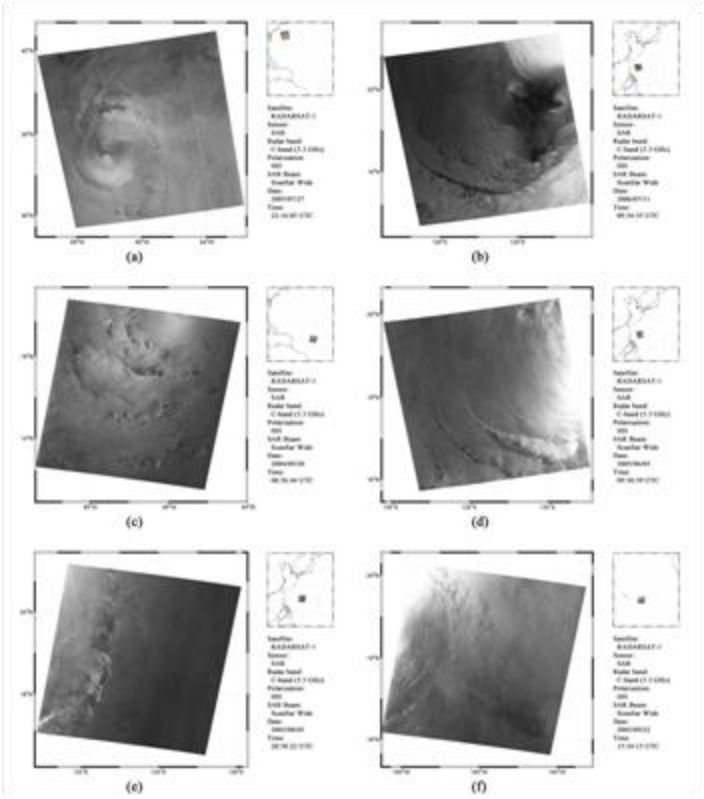

Fig. 5. The geographical positions of the six Tropical cyclones and their wind speed. (a) Tropical cyclone Franklin captured on 22:16:05, July 28th, 2005. (b) Tropical cyclone Bilis captured on 09:34:35, July 11th, 2006. (c) Tropical cyclone Karl captured on 08:56:44, September 20th, 2004. (d) Tropical cyclone Nesat captured on 09:30:39, June 5th, 2005. (e) Tropical cyclone Etau captured on 20:58:22, August 5th, 2003. (f) Tropical cyclone Jova captured on 15:34:15, September 22th, 2005.

is. Suppose that there are N pixels on a skeleton line and we know their inflow angles $\{\alpha_{SR_i}\}$, the fitness function can be defined as:

$$z = \left|\alpha_{SR_i} - \{A_{\alpha 0}(r_i^*, V_{max}) + A_{\alpha 1}(r_i^*, V_s, V_{max}) \cdot cos[\theta_i - P_{\alpha 1}(r_i^*, V_s)] + \varepsilon\}\right| \quad (8)$$

If we do not know the inflow angles, we can change the fitness function. The mean inflow angle in tropical cyclones $\alpha_{average}$ is found to be $-22.6^\circ \pm 2.2^\circ$ (95% confidence) [42], which agrees well with the previous results [48]. Therefore the fitness function can be changed as:

$$z = \left|\frac{\sum_{i=1}^{N}\{A_{\alpha 0}(r_i^*, V_{max}) + A_{\alpha 1}(r_i^*, V_s, V_{max}) \cdot \cos[\theta_i - P_{\alpha 1}(r_i^*, V_s)] + \varepsilon\}}{N} - \alpha_{average}\right| \quad (9)$$

The speed and position of each particle can be changed using formulae (10) and (11).

$$v_i = w \cdot v_{i-1} + c_1 \cdot rand_1 \cdot (pbest_{i-1} - present_{i-1}) + c_2 \cdot rand_2 \cdot (gbest_{i-1} - present_{i-1}) \quad (10)$$

$$present_i = present_{i-1} + v_i \quad (11)$$

where c_1 and c_2 are acceleration coefficients, and $rand_1$ and $rand_2$ are random numbers between 0 and 1.

The optimum solution of (x_c, y_c) can be considered as the center of the tropical cyclone. Sometimes there may be several spiral lines after the extraction of skeleton lines. Each spiral line has an optimal solution. The optimal center achieved by one matching spiral line may not be the optimal solution of another matching spiral line. Theoretically there is a center point which is the compromised optimal solution for all the spiral lines. Hence we take the average of all optima as the final center point.

III. Experimental Results And Discussions

The data used in our experiments are RADARSAT-1 SAR tropical cyclone images. RADARSAT-1 C-band SAR images of tropical cyclones have been acquired worldwide since 1998 to support scientific research through the Hurricane Watch program which is a collaborative program between the National Oceanic and Atmospheric (NOAA), the Canada Centre for Remote Sensing (CCRS) of Natural Resources Canada and the Canadian Space Agency (CSA) [49]. These images are ScanSAR wide beam (SCW) images with a medium resolution of 100 m and a swath of 450 km. They are horizontal-transmit and horizontal-receive (HH polarization) data. The six tropical cyclones and their positions are shown in Fig. 5. Fig. 5(a) contains the full structure of tropical cyclone Franklin while the eye area is fuzzy. Fig. 5(b) – Fig. 5(f) contain the other five partially-covered tropical cyclones in SAR images.

We compute the salient region maps from the denoised images (Fig. 6(b) - Fig. 11(b)). To get a gray value contrast feature map, an image is first divided into patches using a 8×8 sliding window. Each step of the sliding window is half of its length. If the sliding window is too large, there will be a serious blocking effect, and a large number of unrelated areas will be contained in the gray value contrast feature map. If the sliding window is too small, the difference within each patch will not be well presented. In addition, the rain-band regions will be discontinuous and holes will easily appear in the connected domain. These side effects will affect the later extraction of skeleton lines. Then the standard deviation of each patch is calculated and normalized. The larger the standard deviation value, the more context change a patch has. Usually we use a threshold to remainder patches with a large standard deviation value. As shown in Fig. 6(c) - Fig. 11 (c), a gray value contrast feature map can indicate the position of rain bands. The parts with higher pixel values mainly contain rain bands.

Then we make use of orientation information by calculating the Gabor features. The Gabor features of a denoised tropical cyclone SAR image are calculated in four orientations (0^o, 45^o, 90^o, 135^o), and then the Gabor feature map is obtained using a weighted combination of four orientation maps. As shown in Fig. 3, experiments indicate that rain bands are more obvious in the 45^o and 135^o orientation angles. Therefore, to distinguish rain bands from other objects, an orientation map of 45^o and an orientation map of 135^o are given higher weights of 0.4, and an orientation map of 0^o and an orientation map of 90^o are given lower weights of 0.1. As shown in Fig. 6(d) - Fig. 11 (d), the Gabor feature maps indicate the obvious rolling tendency and rain bands with higher pixel values.

We get the final salient region map by a weighted combination of the gray value contrast feature map and the Gabor feature map. As shown in the Fig. 6(e) - Fig. 11 (e), rain bands are salient in the final salient region map. After that, we segment the final salient region maps into binary images. Regions with higher pixel values remain. For some small and unrelated regions in the binary image, we used the two filter criteria mentioned in section 2.2 to select the rain bands regions. As shown in Fig. 6(f) - Fig. 11 (f), small and unrelated regions are deleted. The remaining region appears as long and thin lines, which represent the characteristics of rain bands. However, there are still holes in some rain bands regions so we use the expansion operator to solve this problem. After extracting the skeleton lines, pruning is operated to avoid the influence of burrs. Expansion and pruning can be repeated to make the skeleton lines smoother as shown in Fig. 6(i) - Fig. 11 (i).

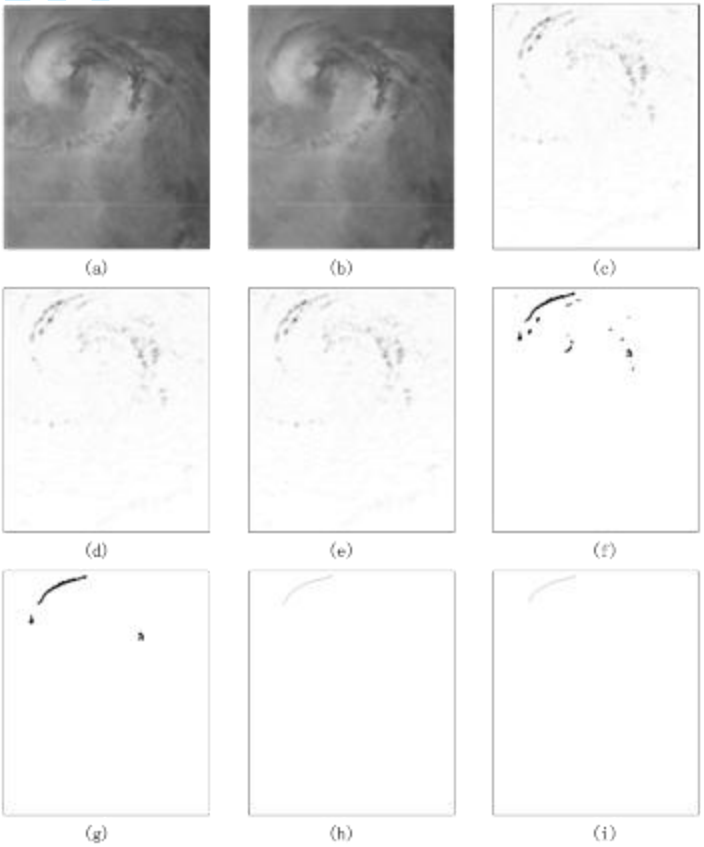

Fig. 6. (a) The SAR image of Tropical cyclone Franklin. (b) The denoised SAR image. (c) The gray value contrast feature map of the denoised SAR image. (d) The Gabor feature map. (e) The salient region map. (f) Remaining regions after selection filter criterion 1. (g) Remaining regions after selection filter criterion 2. (h) The skeleton lines of rain bands. (i) The smooth skeleton lines after pruning.

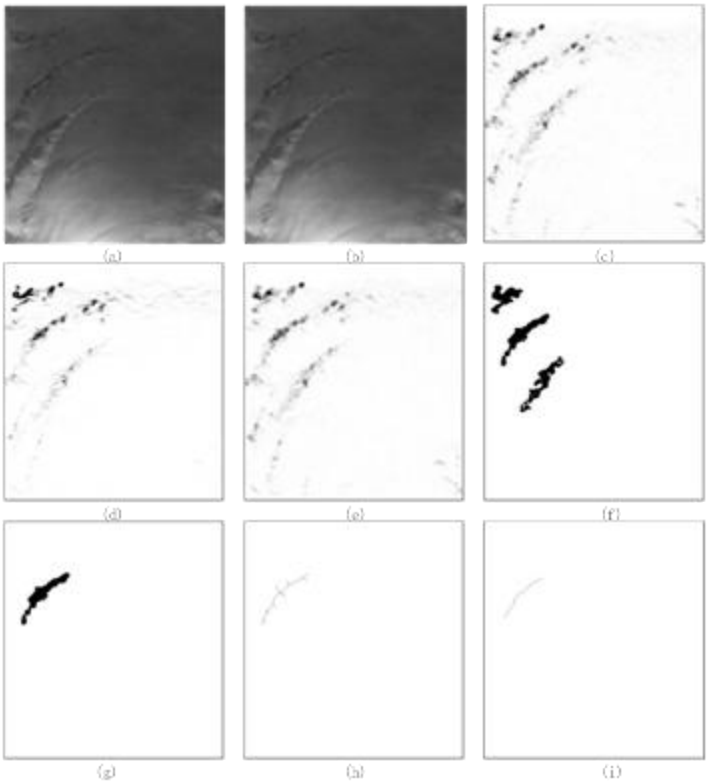

Fig. 7. Results of the SAR image of Tropical cyclone Bilis. Caption of each figure is the same as these in Fig. 6.

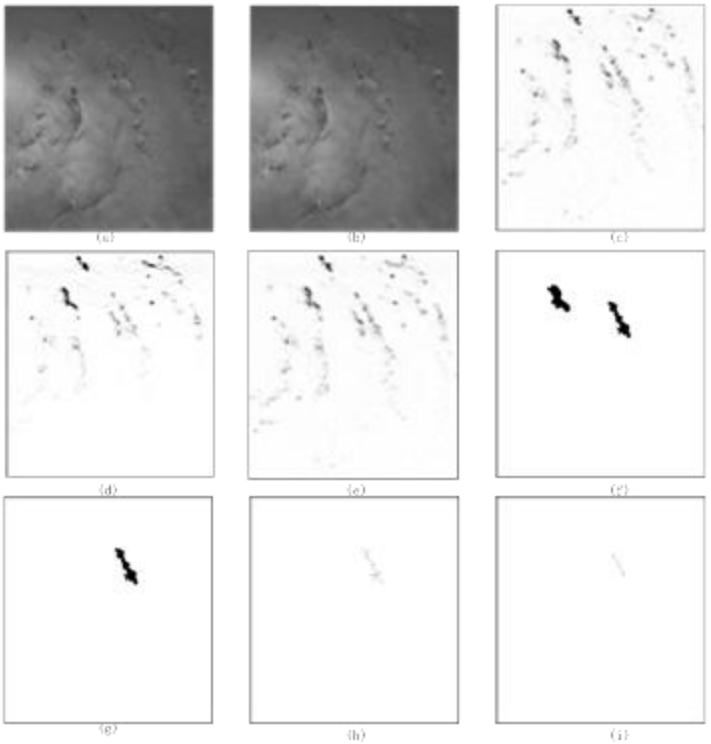

Fig. 8. Results of the SAR image of Tropical cyclone Karl. Caption of each figure is the same as these in Fig. 6.

TABLE II
PROPERTIES ESTIMATED CENTERS WITH OUR METHOD AND CENTERS FROM THE BEST TRACK DATA SETS RECORDS BEFORE AND AFTER THE TIME THAT SAR IMAGES ARE CAPTURED ON. THEORETICALLY THE ESTIMATED CENTER OF A CYCLONE IS BETWEEN THE CENTER POSITIONS ON THE TWO RECORDED TIME.

Tropical cyclone	UTC Time	Estimated center(Lat, Lon)	UTC Time before	Best Track center(Lat, Lon)	UTC Time after	Best Track center(Lat, Lon)
Franklin	2005.07.28 22:16:05	(37.9,-67.2)	2005.07.28 18:00:00	(37.1,-68.0)	2005.07.29 00:00:00	(38.4,-66.6)
Bilis	2006.07.11 09:34:35	(19.5, 128.4)	2006.07.11 06:00:00	(19.1,128.9)	2006.07.11 12:00:00	(19.8,127.9)
Karl	2004.09.20 08:56:44	(17.0, -45.3)	2004.09.20 06:00:00	(17.0, -45.2)	2004.09.20 12:00:00	(17.5, -46.0)
Nesat	2005.06.05 09:30:39	(18.3, 131.3)	2005.06.05 06:00:00	(18.1, 130.9)	2005.06.05 12:00:00	(18.9, 131.3)
Etau	2003.08.05 20:58:22	(19.5, 129.6)	2003.08.05 18:00:00	(20.5, 130.3)	2003.08.06 00:00:00	(21.5, 129.5)
Jova	2005.09.22 15:34:15	(19.7,-148.2)	2005.09.22 12:00:00	(19.4,-147.9)	2005.09.22 18:00:00	(20.1,-148.5)

Finally, using the PSOA, we match each skeleton line with a given model. Here we set $c1 = c2 = 2$ and $w = 1$. The size of the particle is 20 and the number of iterations is 200. The center of a tropical cyclone may be out of the SAR image if there is no eye in the SAR image. Suppose the range of an image is $m \times n$, we expand the search range of PSOA to $3m \times 3n$ or $5m \times 5n$. The initial position and velocity of particles are given randomly. According to the pixel position set $\{(x_i, y_i) | (x_i, y_i) \in l_{ske}\}$ of a skeleton line using the procedures outlined in section 2.4, we calculate the optimal solution of matching with the PSOA. If there are several skeleton lines in a binary image, we calculate the optimal solution of each matching skeleton line and then take an average of all the optima as the final tropical cyclone center. The center location results are shown in Fig. 12. We can see that the centers are within the images in Fig. 12(a) and Fig. 12(b), but the centers are out of the images in the other four figures. We can not estimate whether the results are correct if there are no centers in the SAR images. In order to evaluate the accuracy of our center location results, we compare the estimated center with the NOAA Best Track Data sets in Table 2 and Fig. 13. The NOAA Best Track Data is an archive of global history tropical cyclones since 1842. The information is obtained from NOAA's program "International Best Track Archive for Climate Stewardship (IBTrACS)". The data contain the center position (usually it is the latitude and longitude) and the intensity (described by the maximum wind

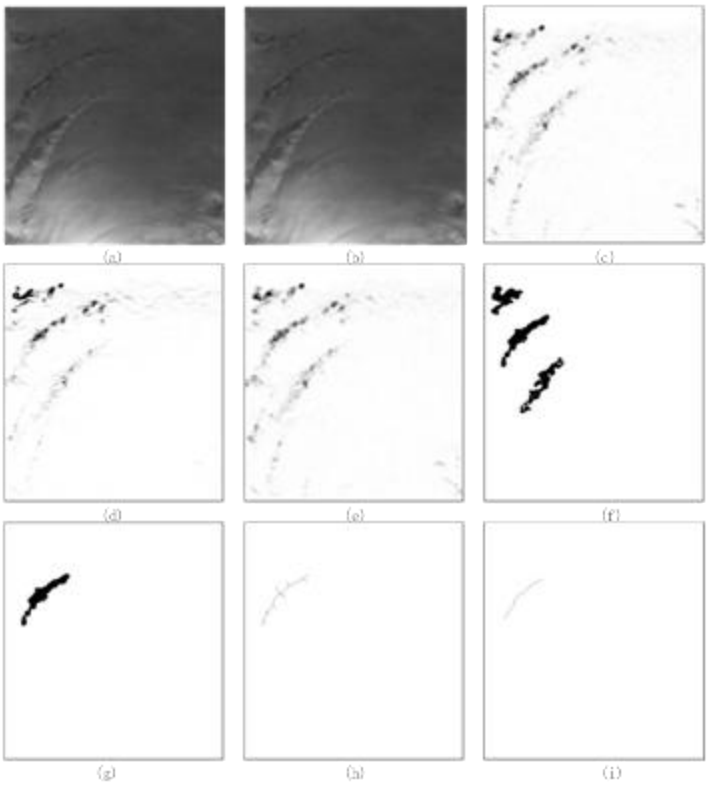

Fig. 9. Results of the SAR image of Tropical cyclone Nesat. Caption of each figure is the same as these in Fig. 6.

speed or the lowest central air pressure) of a tropical cyclone at a certain time and other information. The NOAA Best Track data is updated every six hours. As a result, the locations of the tropical cyclone centers at the SAR imaging times are interpolated from the two nearby Best Track data records. The estimated center position of a tropical cyclone should between the center positions at the two recorded times. Table 2 shows each estimated center's position and the two center positions on the two above recorded times in the best track data set. Using linear interpolation, we draw a straight line between the center positions before and after the time that each SAR image was captured. Then we point out the estimated center position in the same figure. Theoretically the estimated center position should be on the line. We can see that the estimated centers of tropical cyclone Franklin and Bilis are almost on the straight lines, and those of tropical cyclone Karl, Nesat and Jova are close to the straight lines. Their longitude and latitude are respectively within the range of the center position recorded before the imaging time and the position recorded after the image capture time. However, the estimated center position of tropical cyclone Etau is far away from its straight line and its longitude and latitude are a little out of the range. These samples illustrate that our method is effective in most cases but it is not sufficiently good. A large number of experiments prove this. The inflow angle model is proposed based on the analysis of observation data. It is suitable for many tropical cyclones but not all tropical cyclones. In addition, the initialization of particles and the change strategy of particle positions of the PSOA will both affect the optimization results.

In order to prove the accuracy and convergence of the PSOA,

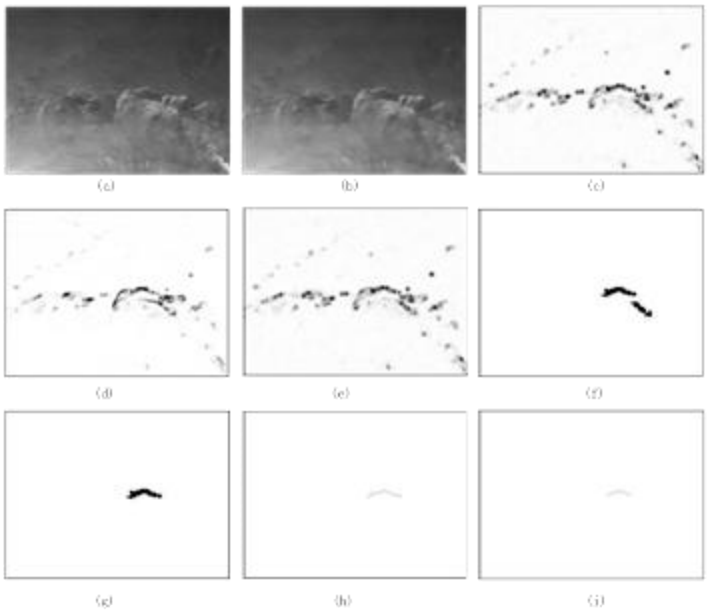

Fig. 10. Results of the SAR image of Tropical cyclone Etau. Caption of each figure is the same as these in Fig. 6.

here we compare the PSOA and another optimization algorithm – the Genetic Algorithm (GA) in our experiments. The GA was proposed by Holland [50] and widely used for optimization problems, artificial intelligence, etc for its robustness and global search ability. Wong *et al.* [19] used the GA to match skeleton lines with a logarithm spiral and achieved good results. The PSOA and the GA have many common features: They both initialize random population, use the evaluation function to measure the quality of the individual, and carry out the next search according to the fitness value achieved by the evaluation function. Parameters are set as follows in experiments: the population size of both the GA and the PSOA is set to 20 and the iteration number is set to 200. The cross probability in the GA is set to 0.9 and the mutated probability is set to 0.01. The acceleration coefficients *c1* and *c2* are both set to 2 and *w* is set to 1 in the PSOA.

Fig. 14 shows that the optimal solution of the PSOA appears at more or less the 20^{th} iteration, while the optimal solution of the GA appears at more or less the 50^{th} iteration. The search performance of the PSOA is much better than that of the GA. That is because the PSOA changes particle positions more randomly and with less complexity than the GA which needs selection, crossover and mutation operators. Besides, pbest and gbest in the PSOA allows particles to inherit more targeted information and the searching and updating always follow the current gbest, searching the optimum solution in the shortest time. All particles in the PSOA follow the current gbest in the search process and they tend to be the same in the later stage. This suggests that the solution can no longer be optimized when it reaches certain accuracy. Different from the PSOA, chromosomes share information in GA, so the whole population moves to the optimum solution uniformly. These comparisons illustrate that the PSOA is simpler to use without adjusting as many parameters as the GA, and it reaches the optimum solution faster. So the PSOA is a better choice if there

is no high precision requirement.

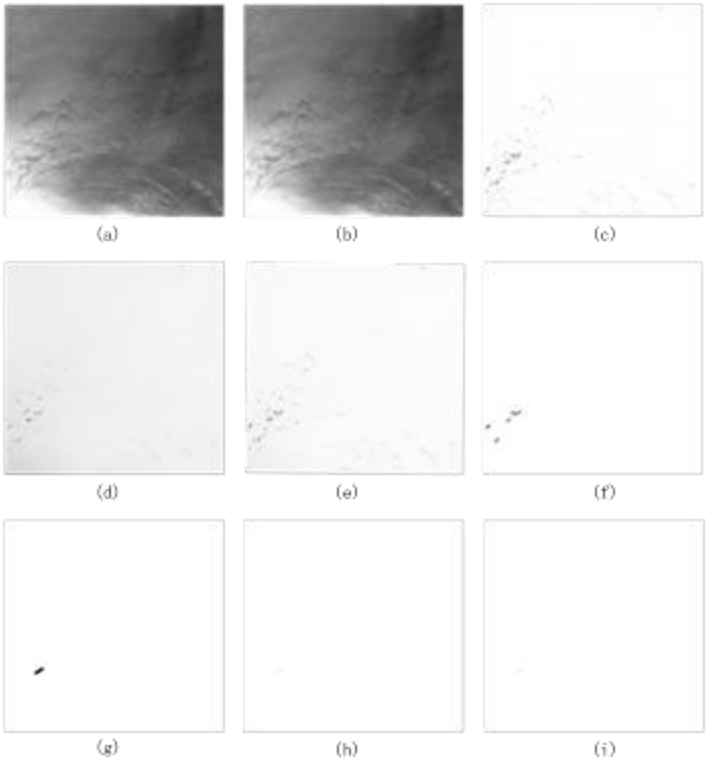

Fig. 11. Results of the SAR image of Tropical cyclone Karl. Caption of each figure is the same as these in Fig. 6.

IV. CONCLUSION

In this paper, we address the problem of the semi-automatic center location of tropical cyclones without eyes in SAR images. In order to get precise matching results with the assistance of spiral rain bands of tropical cyclones, we proposed a location method based on salient region detection and a PSOA for SAR images. Our work contains three main steps: 1) We propose a salient region detection method based on the contrast of gray values and the Gabor features. The final salient region map reflects the spiral structure of rain bands. Rain bands can be effectively extracted with our method. 2) We give two filter criteria to select rain bands that can be used for effective matching. 3) After obtaining the skeleton line of spiral rain bands, we transform the matching problem into an optimization problem and use the PSOA to search the optimum solution. To prove accuracy and convergence, we compare the PSOA results with the GA results. Experiment results show that tropical cyclone centers can be precisely located.

This work is a meaningful attempt to estimate the tropical cyclone center with a single SAR image. It applies to cases that only contain partial structure of a tropical cyclone without eye. It also applies to cases that contain the whole structure of a tropical cyclone with fuzzy eye. It proposes a rain bands extraction method by taking advantage of the pixel gray level contrast between the tropical cyclone and the background and the orientation information in a SAR image. Our experiments indicate that the method is effective in most cases. In practical applications it may be not so effective when there is an island in

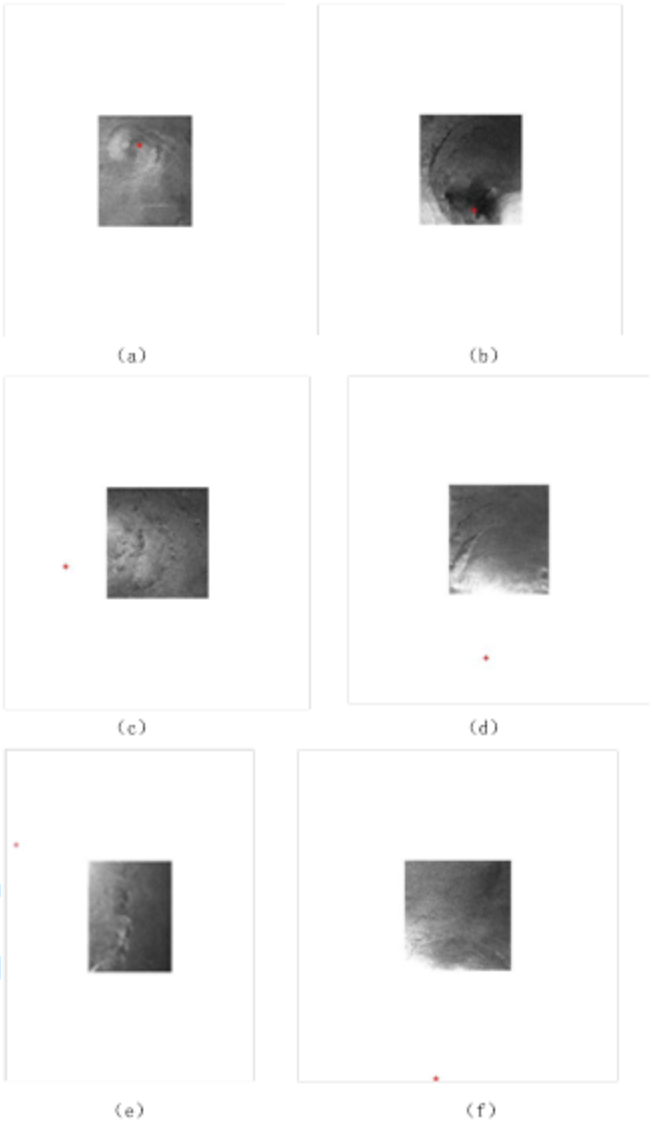

Fig. 12. The center location results of six tropical cyclones. The red * indicates the positions of centers.

the tropical cyclone SAR image or the gray level of the tropical cyclone is close to that of its background. Then the continuous and smooth skeleton lines of rain bands are extracted by two filter criteria and morphologic operations. It is convenient for the following matching problem to use an inflow angle model. It can also use a geometric model such as the logarithmic spiral to match the skeleton lines to solve the center estimation problem [12]-[15]. The two steps can be widely used for tropical cyclone analysis from the view of image processing. All SAR images used in this study are C-band horizontal polarization images. Although L-band (ALOS-1 and -2) and X-band SAR satellites (TerraSAR, Tandem-X, and Cosmo-Skymed) are currently in orbit, the number of images covering tropical cyclones is extremely rare. As a result, we do not have SAR images acquired in other bands to perform similar analyses. However, we believe that the technique developed here can be applied to SAR images acquired at different bands and polarizations.

There are some limitations that we need improve in the

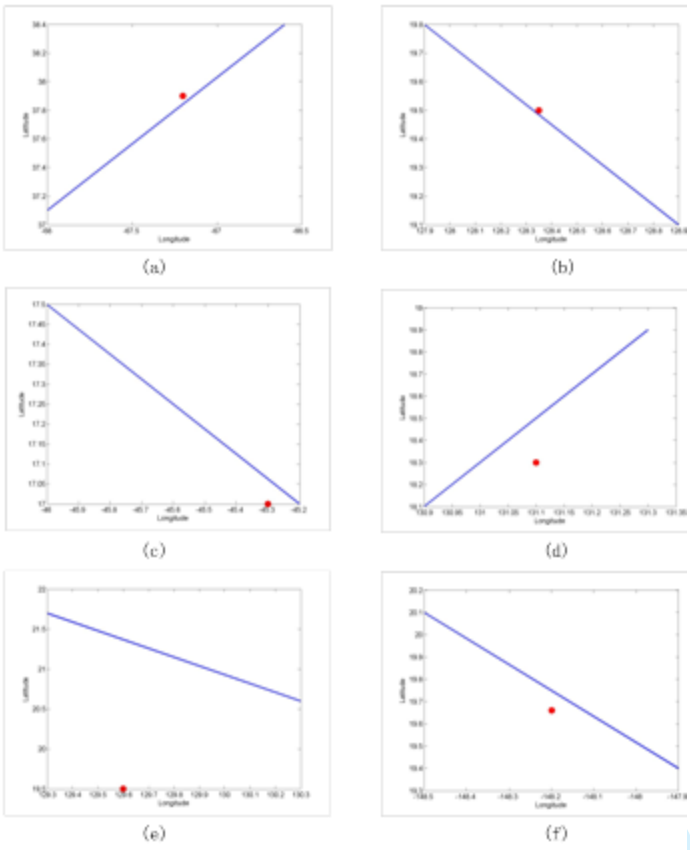

Fig. 13. The position of each estimated center and the straight line between the center positions in the best track data sets recorded before and after the time that the SAR images are captured. Theoretically the estimated center position should be on the straight line. (a) Tropical cyclone Franklin in Fig. 6. (b) Tropical cyclone Bilis in Fig. 7. (c) Tropical cyclone Karl in Fig. 8. (d) Tropical cyclone Nesat in Fig. 9. (e) Tropical cyclone Etau in Fig. 10. (f) Tropical cyclone Jova in Fig. 11.

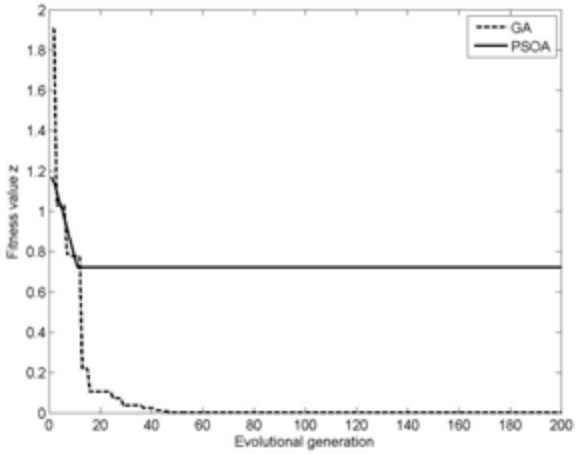

Fig. 14. Fitness values curves of PSOA and GA.

future. We need to adjust several parameters and this means the method will not be fully-automatic. Then an inflow angle model is proposed based on the analysis of near-surface inflow angles using the wind observation data of a number of tropical cyclones. This works well for some tropical cyclones but may not work well for all tropical cyclones. We need to consider the universal applicability of a model. Here we focus on estimating tropical cyclone centers with a single SAR image from the aspect of image processing. It would be interesting to solve this problem by combining other data information such as wind field, image sequence, etc in future studies.

REFERENCES

[1] X. Li, J. A. Zhang, X. F. Yang, W. G.. Pichel, M. D. Maria, D. Long, and Z. W. Li, "Tropical cyclone morphology from spaceborne synthetic aperture radar," *B. Am. Meteorol Soc.*, vol. 94, pp. 215-230, Feb. 2013.
[2] K. Friedman and X. Li, "Storm patterns over the ocean with wide swath SAR," *J Hopkins APL Tech D.*, vol. 21, no.1, pp. 80-85, 2000.
[3] X. Li, "The First Sentinel-1 SAR Image of a Typhoon," Acta Oceanol. Sin., vol. 34, no. 1. pp. 1-2, 2015.
[4] X. Li, W. Pichel, M. He, S. Wu, K. Friedman, P. Clemente-Colon and C. Zhao, "Observation of Hurricane-Generated Ocean Swell Refraction at the Gulf Stream North Wall with the RADARSAT-1 Synthetic Aperture Radar," IEEE Trans. Geosci. Remote Sens., vol. 40, no. 10, 2002.
[5] I. Lee, A. Shamsoddini, X. Li, and J. C. Trinder, "Extracting hurricane eye morphology from spaceborne SAR images using morphological analysis," ISPRS J. of Photogramm. Remote Sens., vol. 7, pp. 115-125, Mar. 2013.
[6] Y. Du and P. W. Vachon, "Characterization of hurricane eyes in RADARSAT-1 images with wavelet analysis," Can. J. Remote Sens., vol. 29, pp. 491-498, 2003.
[7] W. Timothy, Liu, "Progress in scatterometer application," J. Oceanography, vol. 58, pp. 121-136, Feb. 2002.
[8] K. Y. Wong and C. L. Yip, "Tropical cyclone eye fix using genetic algorithm with temporal information," Knowledge-Based Intelligent Information and Engineering Systems, vol. 3681, pp. 854-860, Sep. 2005.
[9] H. Shunsuke and N. Tetsuo, "Estimation of tropical cyclone's intensity using TRMM/TMI brightness temperature data," Journal of the Meteorological Society of Japan, vol. 85, pp. 437-454, 2007.
[10] R. L. Sriver, M. Huber and J. Nusbaumer, "Investigating tropical cyclone-climate feedbacks using the TRMM microwave imager and the quick scatterometer," Geochem Geophys Geosy, vol. 3305, pp. 177-189, 2008.
[11] K.B. Katsaros, P. W. Vachon, W. T . Liu, and P. G. Black. "Microwave remote sensing of tropical cyclones from space," J. Oceanogr, vol. 58. pp. 137-151, Feb. 2002.
[12] J. Horstmann, D. R. Thompson, F. Monaldo, S. Iris, and H. C. Graber. "Can Synthetic Aperture Radars be used to estimate hurricane force winds?" Geophys Res Lett, vol. 32, pp. 1-5, Nov. 2005.
[13] X. F. Yang, X. F. Li, W. G. Pichel, and Z. W. Li, "Comparison of ocean surface winds from ENVISAT ASAR, Metop ASCAT scatterometer, Buoy measurements and NOGAPS model," IEEE T Geosci Remote, vol. 49, pp. 4743–4750, Dec. 2011.
[14] F. Xu, X. F. Li, P. Wang, J, Yang, W. G. Pichel and Y-Q Jin, "A backscattering model of rainfall over rough sea surface for synthetic aperture radar," IEEE T Geosci. Remote, vol. 53, pp. 3042-3054, Feb. 2015.
[15] S. H. Jin, S. Wang, and X. F. Li, "Typhoon eye extraction with an automatic SAR image segmentation method," Int. J Remote Sens., vol. 35, pp. 3978-3993, May. 2014.
[16] G. Zheng, J. S. Yang, A. K. Liu, X. F. Li, W. G. Pichel and S. Y. He, "Comparison of typhoon centers from SAR and IR images and those from best track data sets," IEEE T Geosci. Remote,, vol. 54, pp.1000-1012, Feb. 2016.
[17] P. Wang, C. S. Guo, and Y. X. Luo, "Local spiral curves simulating based on hough transformation and center auto-locating of developing typhoon," Transactions of Tianjin University, vol. 12, pp. 142-146, Apr. 2006.
[18] J. W. Xu, P. Wang, and Y. Y. Xie, "Image segmentation of typhoon spiral cloud bands based on support vector machine," ICML, vol. 2, pp. 1088-1093, Jul. 2009.
[19] K. Y. Wong and C. L. Yip, "Tropical cyclone eye fix using genetic algorithm with temporal information," Knowledge-Based Intelligent Information and Engineering Systems, vol. 3681, pp. 854-860, Sep. 2005.
[20] K. Y. Wong, C. L. Yip, and L. P. Wah, "Automatic tropical cyclone eye fix using genetic algorithm," Expert Syst. Appl., vol. 34, pp. 643-656, 2008.

[21] C. A. Deledalle, L. Denis, and F. Tupin, "Iterative weighted maximum likelihood denoising with probabilistic patch-based weights," IEEE T Image Process, vol. 18, pp. 2661-2672, Aug. 2009.
[22] K. R. Cave and J. M. Wolfe, "Modeling the role of parallel processing in visual search," Cognitive Psychol, vol. 22, pp. 225-271, Apr. 1990.
[23] C. Koch and S. Ullman, "Shifts in selective visual attention: towards the underlying neural circuitry," Matters of Intelligence, vol. 4, pp. 115-141, 1987.
[24] I. Mareschal, J. A. Henrie and R. M. Shapley, "A psychophysical correlate of contrast dependent changes in receptive field properties," Vision Res., vol. 42, pp. 1879-1887, May. 2002.
[25] Y. F. Ma and H. J. Zhang, "Contrast-based image attention analysis by using fuzzy growing," Proceedings of the 11th ACM International Conference on Multimedia, NewYork，2003， pp.374-381.
[26] J. K. Tsotsos, S. M. Culhane, and W. Y. K. Wai, "Modeling visual attention via selective tuning," AI, vol.78, pp.507-545, Oct. 1995.
[27] L. Itti, C. Koch, and E. Niebur, "A model of saliency based visual attention for rapid scene analysis," IEEE Trans. Pattern Anal. Mach. Intell. vol.20, pp. 1254-1259, Nov. 1998.
[28] P. Viola and M. J. Jones, "Robust real-time face detection," IJCV, vol. 57, pp. 137-154, May. 2004.
[29] K. Ehinger, B. Hidalgo-Sotelo, A. Torralba, and A. Oliva, "Modeling search for people in 900 scenes: a combined source model of eye guidance," Vis. Cogn., vol. 17, pp. 945-978, Aug. 2009.
[30] M. Cheng, G. Zhang, N. J. Mitra, X. Huangand S. Hu, "Global contrast based salient region detection," CVPR, pp.409-416, Jun. 2011.
[31] L. Duan, C. Wu, J. Miao, L. Qing, and Y. Fu, "Visual saliency detection by spatially weighted dissimilarity," CVPR, pp. 473-480, Jun. 2011.
[32] T. Liu, J. Sun, N. N. Zheng, and X. O. Tang, "Learning to detect a salient object," CVPR, pp.1-8, Jun. 2007.
[33] W. Kienzle, F. A. Wichmaan, B. Scholkopf, and M O. Frane, "A nonparametric approach to bottom up visual saliency," NIPS, 2007.
[34] P. L. Rosin, "A simple method for detecting salient regions," Pattern Recogn, vol. 42, pp. 2363-2371, Nov. 2009.
[35] S. Goferman, L. Zelnik-Manor, and A. Tal, "Context-aware saliency detection," IEEE T Pattern Anal, vol. 34, pp. 1915-1926, Oct. 2012.
[36] V. Navalpakkam and L. Itti, "An integrated model of top-down and bottom-up attention for optimizing detection speed," CVPR, vol. 2, pp. 2049-2056, 2006.
[37] N. J. Butko and J.R. Movellan, "Optimal scanning for faster object detection," CVPR, pp. 2751-2758, 2009.
[38] J. G. Daugman, "Complete discrete 2d gabor transforms by neural networks for image analysis and compression," IEEE T. Acoust. Speech, vol. 36, pp. 1169-1179, Jul. 1988.
[39] M. Lades, J. C. Vorbruggen, J. Buhmann, J. Lange, C. von der Malsburg, R. P. Wurtz and W. Konen, "Distortion invariant object recognition in the dynamic link architecture," IEEE T. Comput, vol. 42, pp. 300-311, Mar. 1993.
[40] J. Lee, R. M. Haralick and L. G. Shapiro, "Morphologic edge detection," IEEE Journal of Robotics and Automation, vol. 3, pp. 142-156, Apr. 1987.
[41] C. R. Gonzalez and R. E. Woods, "Digital Image Processing(Second Edition)[M]," Publishing House of Electronics Industry, 2002.
[42] J. A. Zhang and E. W. Uhlhorn, "Hurricane sea surface inflow angle and an observation-based parametric model," Am Meteorol Soc., vol. 140, pp. 3587-3605, Nov. 2012.
[43] R. Eberhart and J. Kennedy, "A new optimizer using particle swarm theory," The 6th Int. Symposium on Micro Machine and Human Science, Nagoya, Oct. 1995, pp. 39-43.
[44] R. C. Eberhart and Y. Shi, "Particle swarm optimization: developments, applications and resources," IEEE C. Evol. Computat., vol. 1, pp. 81-86, 2001.
[45] K. Lee and M. EI- Sharkawi, "Fundamentals of particle swarm techniques," IEEE Power Eng. Soc., pp. 71-87, 2008.
[46] H. Yoshida, K. Kawata, Y. Fukuyama, S. Takayama and Y. Nakanishi, "A particle swarm optimization for reactive power and voltage control considering voltage security assessment," IEEE T. Power Syst., vol. 15, pp. 1232-1239, Nov. 2000.
[47] F. van den Bergh and A. P. Engelbrecht, "Training product unit networks using cooperative particle swarm optimisers," IEEE IJCNN, vol. 1, pp. 126-131, Jul. 2001.
[48] M. D. Powell, E. W. Uhlhorn, and J. D. Kepert, "Estimating maximum surface winds from hurricane reconnaissance measurements," Wea. Forecasting, vol. 24, pp. 868–883, Jun. 2009.
[49] S. Banal, S. Iris and R. Saint-Jean, "The Canadian Space Agency's Hurricane Watch Program: supporting research on wind field retrieval from RADARSAT-1 image," Proceedings Ocean SAR, Oct. 2006.
[50] J. H. Holland, "Genetic algorithms and classifier systems: foundations and future applications," Proceedings of the Second International Conference on Genetic Algorithms, pp. 82-89, 1987.